Article

Monolayer SnI$_2$: An Excellent p-Type Thermoelectric Material with Ultralow Lattice Thermal Conductivity

Qing-Yu Xie [1,2], Peng-Fei Liu [1,3], Jiang-Jiang Ma [1,3], Fang-Guang Kuang [4], Kai-Wang Zhang [2,*] and Bao-Tian Wang [1,3,5,*]

1   Institute of High Energy Physics, Chinese Academy of Sciences (CAS), Beijing 100049, China; qyxie@ihep.ac.cn (Q.-Y.X.); pfliu@ihep.ac.cn (P.-F.L.); majj88@ihep.ac.cn (J.-J.M.)
2   School of Physics and Optoelectronics, Xiangtan University, Xiangtan 411105, China
3   Spallation Neutron Source Science Center (SNSSC), Dongguan 523803, China
4   School of Physics and Electronic Information, Gannan Normal University, Ganzhou 341000, China; kuangfg1987@126.com
5   Collaborative Innovation Center of Extreme Optics, Shanxi University, Taiyuan 030006, China
*   Correspondence: kwzhang@xtu.edu.cn (K.-W.Z.); wangbt@ihep.ac.cn (B.-T.W.)

Abstract: Using density functional theory and semiclassical Boltzmann transport equation, the lattice thermal conductivity and electronic transport performance of monolayer SnI$_2$ were systematically investigated. The results show that its room temperature lattice thermal conductivities along the zigzag and armchair directions are as low as 0.33 and 0.19 W/mK, respectively. This is attributed to the strong anharmonicity, softened acoustic modes, and weak bonding interactions. Such values of the lattice thermal conductivity are lower than those of other famous two-dimensional thermoelectric materials such as MoO$_3$, SnSe, and KAgSe. The two quasi-degenerate band valleys for the valence band maximum make it a p-type thermoelectric material. Due to its ultralow lattice thermal conductivities, coupled with an ultrahigh Seebeck coefficient, monolayer SnI$_2$ possesses an ultrahigh figure of merits at 800 K, approaching 4.01 and 3.34 along the armchair and zigzag directions, respectively. The results indicate that monolayer SnI$_2$ is a promising low-dimensional thermoelectric system, and would stimulate further theoretical and experimental investigations of metal halides as thermoelectric materials.

Keywords: thermoelectrics; electronic transport; thermal transport

1. Introduction

With more than 60% of energy in the world lost in the form of waste heat, the thermoelectric system has attracted widespread attention, since it directly converts the waste heat to electric energy through the Seebeck effect. It has the advantages of small size, high reliability, no pollutants, and a feasibility in a wide temperature range. Such a system is widely used in aerospace exploration and industrial production, such as in space probes, thermoelectric generators, and precise temperature controls [1,2]. The converting efficiency of TE materials is ruled by the dimensionless figure of merit (ZT); ZT $= S^2 \sigma T / (\kappa_L + \kappa_e)$, where S, σ, T, κ_L, and κ_e are the Seebeck coefficient, electrical conductivity, absolute temperature, lattice thermal conductivity, and electronic thermal conductivity, respectively. The electronic transport properties S, σ, and κ_e, have a complex coupling relationship, and are difficult to decouple, even though they can be modified via carrier concentration [3–5]. Historically, two aspects were established to enhance ZT: one aspect is to optimize carrier concentration by the band structure, engineered to enhance the power factor (σS^2) [6–9], and the other aspect is to reduce the lattice thermal conductivity, via alloying and nanostructuring [10]. Alternatively, it is more attractive to seek materials with an intrinsic low lattice thermal conductivity (generally associated with complex crystal structures [11]), strong anharmonicity [12,13], lone pair electrons [14,15], and liquid-like behavior [16–18], etc.

The group IVA metal dihalides are candidates for semiconductor optical devices and perovskite solar cells, due to their excellent properties, such as the visible-range band gap and the thickness-dependent band structure [19–22]. However, the application of the Pb-based materials, such as the layered 2H-PbI_2, has been greatly limited by their toxicity and environmental unfriendliness [23–25]. In addition, the surface of the bulk SnI_2 is generally very rough and accompanied by many defects, which strongly scatters carriers [26]. Fortunately, its vdW monolayer has been experimentally realized, via molecular beam epitaxy [27]. The low dimensionality provides an effective conductive channel for carriers, and also suppresses phonon thermal transport [28]. Thus, monolayer SnI_2 is a preferable option over bulk SnI_2 and monolayer PbI_2 in use as a TE material, and deserves to be carefully explored in a systematic study.

In this work, combining first-principles calculations and the semiclassical Boltzmann transport equation, the TE properties of monolayer SnI_2 were systematically explored. Results show that the intrinsic ultralow lattice thermal conductivity originates from the strong anharmonicity, weak bonding, and softened acoustic modes. The Grüneisen parameter, phonons scattering phase space, and phonon relaxation time were calculated to understand the micro-mechanism of the phonon transports. The two quasi-degenerate band valleys for the valence band maximum (VBM) in its electronic band structure led to a p-type TE material. The maximum ZT value along the armchair and zigzag directions at 800 K reach 4.01 and 3.34, respectively, using optimal p-type doping. These results indicate that monolayer SnI_2 exhibits an extraordinary TE response, and is an ideal material for TE applications.

2. Computational Methods

The first-principles calculations were implemented in the Vienna ab initio simulation package (VASP, VASP.5.3, Wien, Austria) [29]. The generalized gradient approximation (GGA) [30,31] in the Perdew–Burke–Ernzerhof (PBE) [32] form was employed to deal with the exchange–correlation functional, with a cutoff of 300 eV on a $9 \times 9 \times 1$ Monkhorst–Pack k-mesh. To screen the interactions between adjacent images, the length of the unit cell of 20 Å was used along the z direction. The geometry structure was fully relaxed, with a criterion of convergence for residual forces of 0.001 eV/Å, and the total energy difference converged to within 10^{-8} eV/Å. To obtain an accurate band gap and electronic transport performance, the Heyd–Suseria–Ernzerhof (HSE06) [33] method was employed.

The electronic transport properties of the monolayer SnI_2 were calculated by solving the semiclassical Boltzmann transport equation, utilizing the BoltzTraP code (Georg K. H. Madsen, Århus, Denmark) [34] with a dense $35 \times 35 \times 1$ k-mesh. The constant relaxation time approach (CRTA) was used, since the relaxation time is not strongly dependent on the energy scale of k_BT, and has accurately predicted TE properties of multitudinous materials. In this work, the electrons relaxation time was calculated using the deformation potential (DP) theory [35], which considers the primarily acoustic phonon scatterings, but ignores effects of the optical phonons in the single parabolic band (SPB) model. Based on the rigid band approximation (RBA) [36] and CRTA, the transport coefficients S, σ, and κ_e can be obtained by:

$$S = \frac{ek_B}{\sigma} \int \Xi(\varepsilon)\left(-\frac{\partial f_0}{\partial \varepsilon}\right)\frac{\varepsilon - u}{k_B T} d\varepsilon \tag{1}$$

$$\sigma = e^2 \int \Xi(\varepsilon)\left(-\frac{\partial f_0}{\partial \varepsilon}\right)\frac{\varepsilon - \mu}{k_B T} d\varepsilon \tag{2}$$

$$\kappa_e = \kappa_0 - \sigma S^2 T = L\sigma T \tag{3}$$

$$\Xi = \sum \nu_k \nu_k \tau_k \tag{4}$$

where k_B, f_0, and $\Xi(\varepsilon)$ are the Boltzmann constant, the Fermi–Dirac distribution function, and the transport distribution function, respectively. The calculation of the relaxation time τ was extremely difficult, due to the various complex scattering mechanism in the crystals. The relaxation time was calculated based on the DP theory in the SPB model,

which considers the predominant scatterings between carriers and acoustic phonons in the low-energy region. In fact, the scattering matrix element ($\left| M(\vec{k}, \vec{k'}) \right|^2$) of the acoustic phonons in the long-wavelength can be approximated as $k_B T E_1^2 / C_{ii}$, where C_{ii} and E_1 are the elastic and DP constants, respectively. Thus, for the 2D material, the carrier mobility and electrons relaxation time can be approached as [37,38]

$$\mu_{2D} = \frac{eh^3 C_{ii}}{8\pi^3 k_B T m_d m * E_1^2} \tag{5}$$

$$\tau = \frac{um^*}{e} \tag{6}$$

where h, m^*, and m_d are the Planck constant, the effective mass along the transport direction, and the averaged effective mass, respectively.

The harmonic second-order interaction force constants (2nd IFCs) and phonon spectrum were calculated using the Phonopy package [39], using a $2 \times 2 \times 1$ supercell with a $5 \times 5 \times 1$ k-mesh using the finite-difference method [40]. The anharmonic third-order interaction force constants (3rd IFCs), which consider the interactions between the sixth-nearest-neighbor atoms, were obtained using the ShengBTE package (ShengBTE version 1.0.2, Wu Li, Grenoble, France; Phonopy version 2.11.0, Atsushi Togo, Sakyo, Japan) [41] with the same supercell. The lattice thermal conductivity and phonon transport properties were obtained using the self-consistent iterative solution of the Boltzmann transport equation, with a dense $36 \times 36 \times 1$ mesh, which had a good convergence. Based on the Boltzmann transport equation, with the Fourier's low of heat conduction, the matrix elements of the phonon thermal conductivity can be expressed by [42,43]

$$\kappa_{p.\alpha\beta} = \frac{1}{N_q} \sum_{\lambda} c_{\lambda} v_{\lambda,\alpha} v_{\lambda,\beta} \tau_{\lambda} \tag{7}$$

where α and β are the Cartesian indices, N_q is the total number of q-points sampled in the first Brillouin zone, and c_{λ}, v_{λ}, and τ_{λ} are the mode-specific heat capacities, phonon group velocity, and the relaxation time, respectively. Here, the phonon thermal properties were calculated based on the 3rd IFCs, ignoring the fourth- and higher-order terms. This strategy described the phonon behavior of the most anharmonic materials [44,45]. To define the effective thickness of two-dimensional (2D) materials, the summation of interlayer distance and the vdW radii of the outermost surface atoms was adopted [44].

3. Results and Discussion

3.1. Geometry and Electronic Structure

Monolayer SnI$_2$ crystallizes in a hexagonal lattice with space group P-3m1 (164), as shown in Figure 1. The optimized lattice parameter is 4.57 Å, which is in good agreement with the previous experimental data of 4.48 Å [27]. The structure is analogous to H-MoS$_2$ [46], consisting of three layers, with Sn atoms as the middle layer, and I atoms as the upper and lower atomic layers. The electron localization function (ELF) provides a deeper insight to characterize the nature of, and strengthen, the chemical band. Figure 1c shows the calculated three-dimensional (3D) ELF map (isosurface level of 0.97). The ELF around I is in the shape of a "mushroom", suggesting the existence of the lone pair electrons. Moreover, the electron sharing is better visualized by the 2D ELF map in Figure 1d. The interstitial electrons between Sn and I are close to I atoms, and the value of the area between them is 0.5, which shows the characteristics of a free electron gas and indicates a weak bonding between Sn and I atoms. The electronic repulsion between the lone pair electrons and the Sn–I bonding electrons results in strong anharmonicity, such as in CuSbS$_2$ [14]. The complex structure and lone pair electrons are also beneficial to its low lattice thermal conductivity.
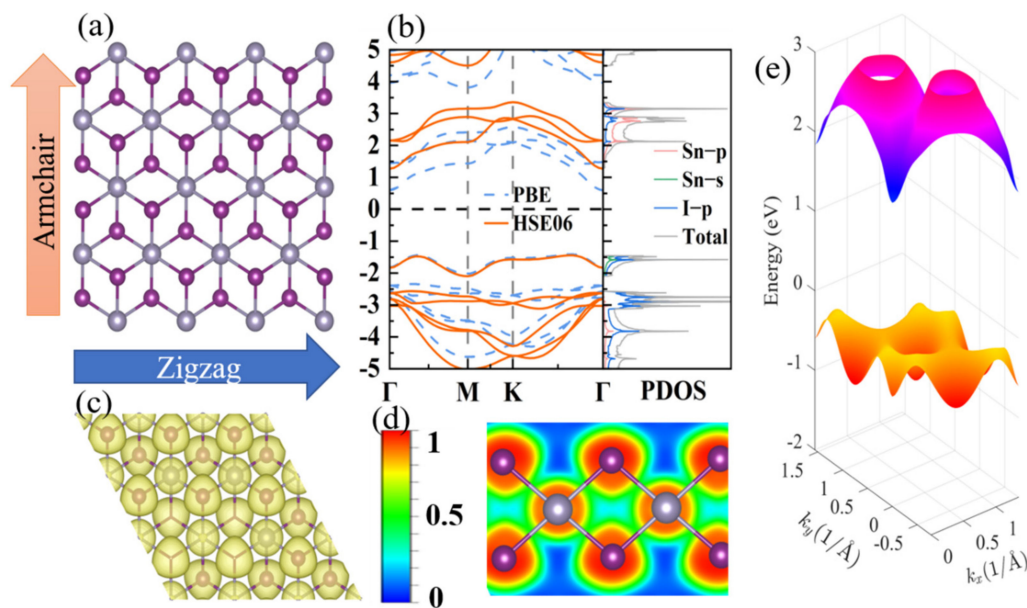
Figure 1. (**a**) Top view of the atomic structure of SnI_2 monolayer. (**b**) The electronic band structures calculated with PBE and HSE06 hybrid functional potentials. (**c**,**d**) the 3D and 2D ELF maps. (**e**) The 3D electronic band structure calculated with PBE.

The electronic structure plays a crucial role in characterizing the electronic transport properties. As shown in Figure 1b, the electronic band structures obtained from the PBE and HSE06 hybrid function potentials are presented. They exhibit analogous band structures, except for a more accurate bandgap (2.71 eV) that approaches the experiment value (2.9 eV) [27] for the latter structure. The conduction band mainly originates from the *p* orbitals of the Sn atom and the *p* orbitals of the I atom, whereas the valence band consists of the *s* orbital of the Sn atom and the *p* orbitals of the I atom. Below the VBM, there are two quasi-degenerate band valleys along the Γ–M and Γ–K directions with an energy difference of ~0.03 eV, which is far less than those in SnTe (~0.35 eV) [47] and PbTe (~0.15 eV) [1]. The multi-energy valley enhances the TE performance and is verified in many materials [48,49]. However, the behavior of band valleys degenerate do not exist for the conduction band minimum (CBM), which is located at the Γ point. Hence, it is expected that the TE performance of the p-type could be superior to that of the n-type.

3.2. Electronic Transport Properties

All the parameters for electronic transport, calculated according to the DP theory, are tabulated in Table 1. Based on the reasonable relaxation time, all the electronic transport coefficients, Seebeck coefficient *S*, electrical conductivity σ, and power factor (PF), as a function of temperature at the corresponding optimal carrier concentration for p-type SnI_2, range from 1×10^{13} to 1×10^{14} cm^{-2}, and are presented in Figure 2a–c. For comparison, those for n-type SnI_2 at the same condition are also plotted in Figure 2d–f. Here, the tiny anisotropy characteristics are ignored.

Table 1. The calculated DP constant E_1, elastic constant, effective mass, carrier mobility, and relaxation time along the zigzag and armchair directions in monolayer SnI_2 at 300 K.

Direction	Type	E_1 (eV)	C_{ii} (J/m^2)	m^* (m_0)	u (cm^{-2}V^{-1}S^{-1}))	τ (fs)
Zigzag	e	−4.44	17.92	0.59	42.52	17.41
	h	−4.43	17.92	0.73	40.16	16.72
Armchair	e	−4.25	17.42	0.84	30.48	15.17
	h	−4.49	17.42	0.68	35.14	13.60
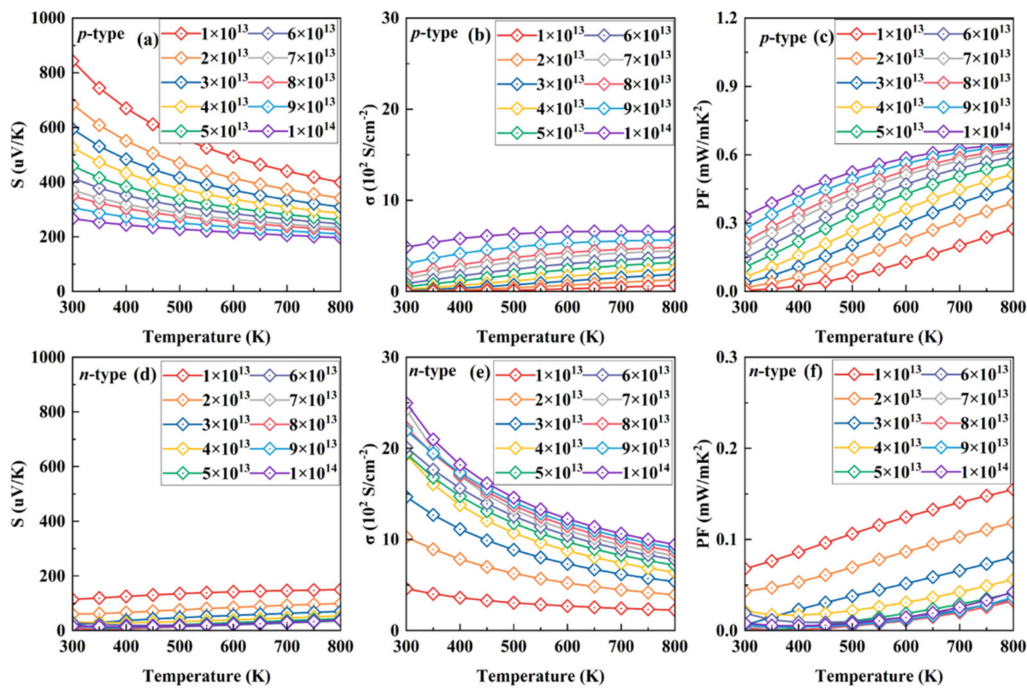
Figure 2. Seebeck coefficient, electronic conductivity, and PF as a function of temperature under various concentrations of p- (**a**–**c**) and n-type (**d**–**f**) doping.

Increasing the carrier concentration, the chemical potential enters in the deeper energy levels for both p- and n-types of SnI_2, resulting in a decreased Seebeck coefficient at the same temperature. It is clear that the values under p-type doping are always far larger than those under n-type at the same condition, which can be attributed to the multi-band character near the VBM, as shown in Figure 1b. For example, the absolute values of the S under p- and n-types of doping at 700 K are 439 and 146 uV/K, respectively, for a doping concentration of 1×10^{13} cm^{-2}. In addition, the trend of S under p-type doping is opposite to that under n-type. The former decreases while the latter increases upon heating.

Compared with S, the electronic conductivity σ exhibits a different behavior, due to the complete relationship between them, as Equations (1) and (2) show. Interestingly, in all cases, the electrical conductivities for p-type SnI_2 are always far less than those for n-type. For example, the values under p- and n-type doping are 0.46 and 2.43 S/cm^{-2}, respectively, at 700 K for a doping concentration of 1×10^{13} cm^{-2}. At 800 K, the electrical conductivity under p-type (n-type) increases from ~0.67 S/cm^{-2} (~2.24 S/cm^{-2}) for 1×10^{13} cm^{-2} to 6.35 S/cm^{-2} (9.43 S/cm^{-2}) for 1×10^{14} cm^{-2}.

Ultimately, the PF decouples the complete relationship between the Seebeck coefficient and electrical conductivity. It is clearly seen that the p-type SnI_2 possesses significantly higher PF values than those of the n-type system. This is in good agreement with the previous analysis for the electronic structure. At 800 K, the PF for p-type increases from ~0.27 mW/mK^2 for 1×10^{13} cm^{-2} to 0.62 mW/mK^2 for 1×10^{14} cm^{-2}. For the n-type system, however, the PF decreases from ~0.15 mW/mK^2 for 1×10^{13} cm^{-2} to 0.04 mW/mK^2 for 1×10^{14} cm^{-2}. Thus, it is expected that the p-type SnI_2 possesses a more excellent performance than that of the n-type. According to the Wiedemann–Franz law, $\kappa_e = L\sigma T$, where L is the Lorenz number, the classical value L = $(\pi k_B)^2/3e^2 \approx 2.44 \times 10^{-8}$ WΩK^{-2} is adopted. This value meets the result of κ_0-$\sigma S^2 T$ [50]. Thus, the electronic conductivity is proportional to the electronic thermal conductivity. The results in the present work also obey this rule.

3.3. Phonon Transport Properties

As shown in Figure 3a, the calculated total κ_L is very low in the wide temperature of 300–800 K. Remarkably, the low room temperature phonon thermal conductivities of

0.33 and 0.19 W/mK along the armchair and zigzag directions, respectively, are fundamentally lower than those previously reported values for 2D MO_3 (1.57 W/mk) [51], SnSe (2.77 W/mK) [13], and CaP_3 (0.65 W/mK) [52]. Through analyzing the contributions of the acoustic phonon branches along the in-plane (TA and LA) or out-of-plane (ZA), as well as the optical phonon modes to the total κ_L, results show that the main contribution to the κ_L is from the ZA mode. In the following, we reveal the origins of such ultralow phonon conductivity, and present a comprehensive analysis to support this result.
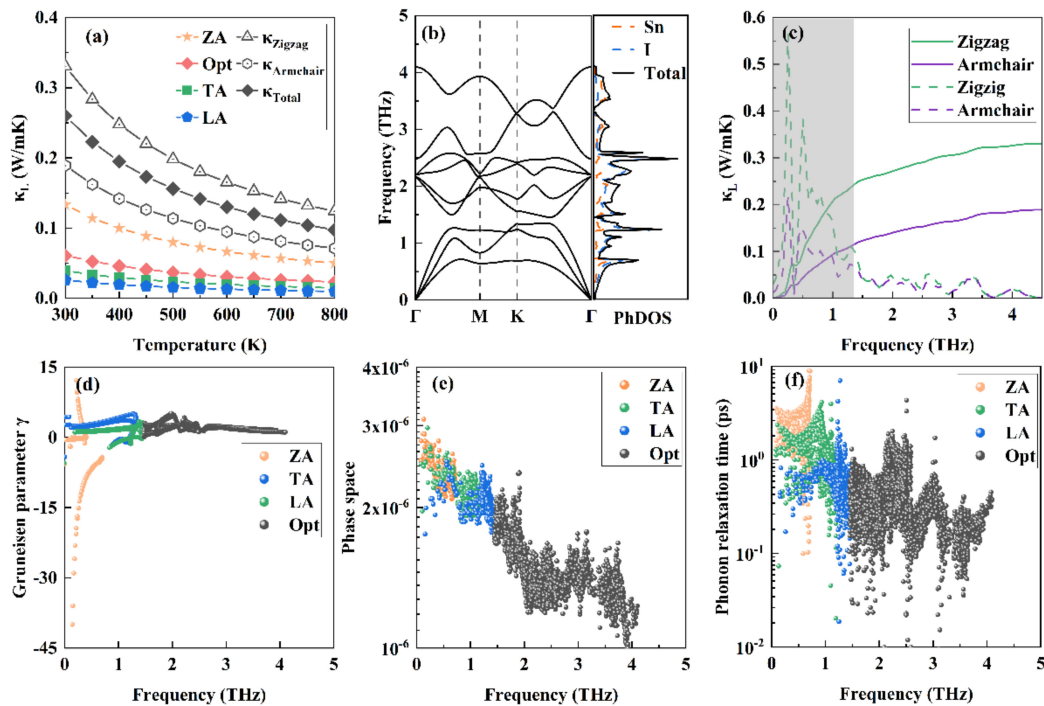
Figure 3. (**a**) Calculated lattice thermal conductivity. The contributions from the ZA, TA, LA, and optical modes to the total κ_L, as well as the lattice thermal conductivities along the armchair and the zigzag directions, are shown. (**b**) Phonon dispersion curves and corresponding PhDOS. (**c**) Cumulative thermal conductivity and the derivatives (dashed line) with respect to frequency. (**d–f**) Grüneisen parameter γ, phonon scattering phase space, and phonon relaxation time of the ZA, TA, LA, and optical modes.

The phonon dispersion curves are presented in Figure 3b. With three atoms in its primitive cell, there are three acoustic and six optical phonon modes for monolayer SnI_2. It is dynamically stable, since no imaginary frequency is observed. Near the long wave limit, the TA and LA branches are in linear trend, whereas the ZA branch exhibits a quadratic trend. These features are typical for 2D materials, and can be explained with the elastic theory of thin plate [53]. It is clearly seen that a narrow phonon gap of about 0.1 THz separates the phonon modes into the acoustic phonon part (0~1.35 THz) and the optical phonon part (1.45~4.10 THz). The cutoff acoustic phonon frequency, which is as low as 1.35 THz, is lower than those for SnSe (1.6 THz) and SnS (1.9 THz) [13]. The low-lying acoustic modes, as well as the soft mode for TA near the M point, imply the weak bonding between Sn and I atoms, consistent with the previous analysis. From the corresponding phonon density of states (PhDOS), the contributions from the I atomic vibrations are apparently larger than those from Sn, within the region of 2.8 to 4.10 THz. Both Sn and I evidently contribute in a wide energy range, implying the nature of covalent bonding [12]. In addition, it is recalled that the decoupling of the in-plane and out-of-plane phonon modes results in ultrahigh phonon thermal conductivity for graphene, due to its one atom plane nature [53,54]. However, such full decoupling behavior should not be observed for a finite thickness 2D system, such as the case of the present studied monolayer SnI_2.

To explain the anomalous thermal transport behavior of monolayer SnI_2, the cumulative lattice conductivity, and their derivatives, with respect to frequency at 300 K are calculated and presented in Figure 3c. Clearly, the κ_L is mainly caused by phonons of the cutoff acoustic part (the shadow region < 1.35 THz). Specifically, the contributions from ZA, TA, LA, and the optical branches are 51.21%, 15.14%, 10%, and 23.54%, respectively. For graphene, the low frequency (0–5 THz) also dominates the κ_L and the ZA mode, and contributes 75% to κ_L [54]. Comparing with graphene, the structure of the monolayer SnI_2 lacks mirror symmetry. Thus, the mirror symmetry does not reflect whether the ZA mode dominates the thermal transport [55].

Generally, there are two factors that dominate the κ_L: (i) anharmonic interaction matrix elements, and (ii) the inverse of phonon phase space volume. The Grüneisen parameter γ is generally employed to quantify the strength of anharmonicity [41]. Figure 3d shows the calculated γ of the ZA, TA, LA, and optical modes of the SnI_2 monolayer. As a large $|\gamma|$ implies strong anharmonicity, it can be seen that the ZA mode exhibits giant anharmonicity. The large $|\gamma|$ of this out-of-plane mode means that the anharmonicity of the bonding between Sn and I atoms in the vertical direction of the monolayer plate is strong. The phonon scattering phase space reveals all available scattering processes, which are ruled by the energy and (quasi)momentum conservation. As shown in Figure 3e, the total scatting phase space of the ZA, TA, and LA modes are 1.55×10^{-3}, 1.41×10^{-3}, and 1.35×10^{-3}, respectively, which confirms more abundant scattering channels of the ZA mode, than those of the TA and LA modes. The larger the phonon phase space, the greater the contribution to the κ_L, thus, validating the decreasing contributions to κ_L from the ZA, TA, and then LA modes. The phonon relaxation time provides a deeper microcosmic insight to understand the ultralow κ_L of SnI_2. Compared with the monolayer SnP_3 [38], monolayer SnI_2 possesses a shorter phonon relaxation time, implying an ultralow κ_L.

3.4. Thermoelectric Figure of Merit

By combining the phonon and electron transport coefficients, the ZT of SnI_2 under p- and n-types of doping as functions of temperature and carrier concentration are presented in Figure 4. Owing to the calculated thermal conductivity, along the zigzag direction is slightly larger than the armchair direction, and it is expected that the ZT along the armchair direction is higher than that along the zigzag direction. In addition, the p-type SnI_2 is obviously superior to the n-type, since the two quasi-degenerate band valleys in VBM leads to a larger Seebeck coefficient. Results show that monolayer SnI_2 is thermally stable up to 800 K, by performing ab initio molecular dynamic (AIMD) simulations (see Figure S1). The values of ZT are as high as 4.01 and 3.34 along the armchair and zigzag directions, respectively, around concentrations of 1.0×10^{13} and 1.2×10^{13} cm^{-2}, at 800 K. Such large values are better than the experimental value of 2.6 for the well-known TE material SnSe along the specific axis at 925 K [3]. In addition, the doping carrier concentrations at such levels have been realized experimentally in monolayer MoS_2 [56]. Therefore, such a high TE value for monolayer SnI_2 is possible, and indicates its excellent potential TE performance.
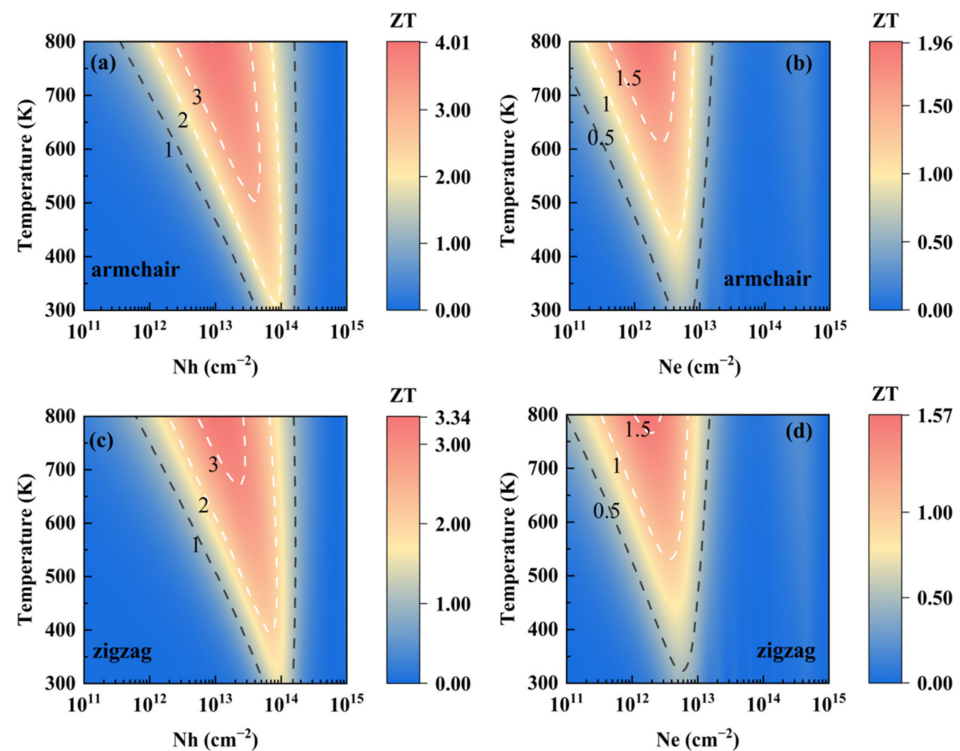
Figure 4. Contour maps of ZT as functions of both temperature and carrier concentration for monolayer SnI_2: (**a**) p-type and (**b**) n-type along the armchair direction, (**c**) p-type and (**d**) n-type along the zigzag direction.

To clearly compare the TE performances of the monolayer SnI_2 with some famous TE materials, the κ_L and the max ZT are listed in Table 2. According to these results, the monolayer SnI_2 is an emerging candidate for TE devices, due to its ultrahigh ZT. As seen, the κ_L of monolayer SnI_2 is very low, almost a twentieth of the monolayer SnP_3 [38], and is greatly lower than those of tin selenide and tin sulfide [13,48]. Such low value of the κ_L for monolayer SnI_2 make it a typical 2D TE system. After all, the electronic transport properties can be easily modulated in experiments, while the lattice thermal conductivity is very difficult to change. In addition, the κ_L values at the level of 0.1–0.5 W/mK in experiments are very few. To the best of our knowledge, the complex systems of $CsAg_5Te_3$ (0.18 W/mK) [57] and $CsCu_5Se_3$ (0.4~0.8 W/mK) [58], as well as the bulk superlattice material $Bi_4O_4SeCl_2$ (0.1 W/mK) [59], are typical low κ_L TE materials. Overall, the low thermal conductivity, as well as the high ZT, make monolayer SnI_2 a good TE material for low-dimensional devices.

Table 2. κ_L at 300 K and the max ZT at corresponding maximum thermodynamic temperature for monolayer SnI_2, as well as some typical TE materials.

Material	κ_L (W/mK)	ZT	
SnI_2	0.26	4.01 (800 K)	This work
SnS	1.5	1.00 (750 K)	Ref. [13]
SnSe	0.6	1.50 (750 K)	Ref. [13]
SnP3	4.97	3.46 (500 K)	Ref. [38]
SnSe	1.12	0.85 (900 K)	Ref. [48]
LaCuOSe	0.84	2.71 (900 K)	Ref. [50]

4. Conclusions

In summary, the TE properties of monolayer SnI_2 were studied using DFT and the semi-classical Boltzmann transport equation. The results indicate that this 2D material possesses intrinsically ultralow lattice thermal conductivity. Its strong anharmonicity, weak

bonding, and softened acoustic branches greatly suppress the phonon transport, and result in an ultralow κ_L of 0.33 and 0.18 W/mK at 300 K along the zigzag and armchair directions, respectively. The p-type SnI_2 possesses a superior electric transport performance than the n-type one, due to the two quasi-degenerate band valleys in its VBM. The ZT at 800 K under p-type doping is as high as 4.01 along the armchair direction. Collectively, these results indicate the great advantages of monolayer SnI_2 for converting heat energy with high efficiency at high temperatures. Generally, when the ZT value of a material exceeds 1.0, it is considered as an ideal TE material. Therefore, the high ZT of monolayer SnI_2 demonstrates it as an emerging candidate for TE applications.

Supplementary Materials: The following supporting information can be downloaded at: https://www.mdpi.com/article/10.3390/ma15093147/s1, Figure S1: Free energy fluctuations with respect to time and equilibrium structures of SnI2 monolayer by AIMD simulations at 800 K.

Author Contributions: Conceptualization, Q.-Y.X., K.-W.Z. and B.-T.W.; methodology, Q.-Y.X., P.-F.L., J.-J.M. and B.-T.W.; software, B.-T.W.; validation, Q.-Y.X., K.-W.Z. and B.-T.W.; formal analysis, Q.-Y.X.; investigation, Q.-Y.X., P.-F.L. and F.-G.K.; resources, B.-T.W.; data curation, Q.-Y.X. and B.-T.W.; writing—original draft preparation, Q.-Y.X.; writing—review and editing, K.-W.Z. and B.-T.W.; supervision, K.-W.Z. and B.-T.W.; project administration, K.-W.Z. and B.-T.W.; funding acquisition, B.-T.W. All authors have read and agreed to the published version of the manuscript.

Institutional Review Board Statement: Not applicable.

Informed Consent Statement: Not applicable.

Data Availability Statement: The data presented in this study are available on request from the corresponding authors. The data are not publicly available due to ongoing research in the project.

Conflicts of Interest: There are no conflicts to declare.

References

1. Pei, Y.; Shi, X.; LaLonde, A.; Wang, H.; Chen, L.; Snyder, G.J. Convergence of electronic bands for high performance bulk thermoelectrics. *Nature* **2011**, *473*, 66–69. [CrossRef] [PubMed]
2. Tan, G.; Zhao, L.D.; Kanatzidis, M.G. Rationally Designing High-Performance Bulk Thermoelectric Materials. *Chem. Rev.* **2016**, *116*, 12123–12149. [CrossRef] [PubMed]
3. Zhao, L.D.; Tan, G.; Hao, S.; He, J.; Pei, Y.; Chi, H.; Wang, H.; Gong, S.; Xu, H.; Dravid, V.P.; et al. Ultrahigh power factor and thermoelectric performance in hole-doped single-crystal SnSe. *Science* **2016**, *351*, 141–144. [CrossRef] [PubMed]
4. Zhang, X.; Zhao, L.-D. Thermoelectric materials: Energy conversion between heat and electricity. *J. Mater.* **2015**, *1*, 92–105. [CrossRef]
5. Zhao, L.D.; Chang, C.; Tan, G.J.; Kanatzidis, M.G. SnSe: A remarkable new thermoelectric material. *Energy Environ. Sci.* **2016**, *9*, 3044–3060. [CrossRef]
6. Zhao, L.D.; He, J.; Wu, C.I.; Hogan, T.P.; Zhou, X.; Uher, C.; Dravid, V.P.; Kanatzidis, M.G. Thermoelectrics with earth abundant elements: High performance p-type PbS nanostructured with SrS and CaS. *J. Am. Chem. Soc.* **2012**, *134*, 7902–7912. [CrossRef]
7. Zhao, L.D.; Wu, H.J.; Hao, S.Q.; Wu, C.I.; Zhou, X.Y.; Biswas, K.; He, J.Q.; Hogan, T.P.; Uher, C.; Wolverton, C.; et al. All-scale hierarchical thermoelectrics: MgTe in PbTe facilitates valence band convergence and suppresses bipolar thermal transport for high performance. *Energy Environ. Sci.* **2013**, *6*, 3346–3355. [CrossRef]
8. Pei, Y.Z.; May, A.F.; Snyder, G.J. Self-Tuning the Carrier Concentration of PbTe/Ag_2Te Composites with Excess Ag for High Thermoelectric Performance. *Adv. Energy Mater.* **2011**, *1*, 291–296. [CrossRef]
9. Zebarjadi, M.; Joshi, G.; Zhu, G.; Yu, B.; Minnich, A.; Lan, Y.; Wang, X.; Dresselhaus, M.; Ren, Z.; Chen, G. Power factor enhancement by modulation doping in bulk nanocomposites. *Nano Lett.* **2011**, *11*, 2225–2230. [CrossRef]
10. Shi, X.; Yang, J.; Salvador, J.R.; Chi, M.; Cho, J.Y.; Wang, H.; Bai, S.; Yang, J.; Zhang, W.; Chen, L. Multiple-filled skutterudites: High thermoelectric figure of merit through separately optimizing electrical and thermal transports. *J. Am. Chem. Soc.* **2011**, *133*, 7837–7846. [CrossRef]
11. Zhang, Y.; Skoug, E.; Cain, J.; Ozoliņš, V.; Morelli, D.; Wolverton, C. First-principles description of anomalously low lattice thermal conductivity in thermoelectric Cu-Sb-Se ternary semiconductors. *Phys. Rev. B* **2012**, *85*, 054306. [CrossRef]

12. Liu, P.-F.; Bo, T.; Xu, J.; Yin, W.; Zhang, J.; Wang, F.; Eriksson, O.; Wang, B.-T. First-principles calculations of the ultralow thermal conductivity in two-dimensional group-IV selenides. *Phys. Rev. B* **2018**, *98*, 235426. [CrossRef]

13. Guo, R.Q.; Wang, X.J.; Kuang, Y.D.; Huang, B.L. First-principles study of anisotropic thermoelectric transport properties of IV-VI semiconductor compounds SnSe and SnS. *Phys. Rev. B* **2015**, *92*, 115202. [CrossRef]

14. Feng, Z.Z.; Jia, T.T.; Zhang, J.H.; Wang, Y.X.; Zhang, Y.S. Dual effects of lone-pair electrons and rattling atoms in $CuBiS_2$ on its ultralow thermal conductivity. *Phys. Rev. B* **2017**, *96*, 235205. [CrossRef]

15. Nielsen, M.D.; Ozolins, V.; Heremans, J.P. Lone pair electrons minimize lattice thermal conductivity. *Energy Environ. Sci.* **2013**, *6*, 570–578. [CrossRef]

16. Liu, H.; Yuan, X.; Lu, P.; Shi, X.; Xu, F.; He, Y.; Tang, Y.; Bai, S.; Zhang, W.; Chen, L.; et al. Ultrahigh thermoelectric performance by electron and phonon critical scattering in $Cu_2 Se_{1-x} I_x$. *Adv. Mater.* **2013**, *25*, 6607–6612. [CrossRef]

17. Wu, B.; Zhou, Y.; Hu, M. Two-Channel Thermal Transport in Ordered-Disordered Superionic Ag_2Te and Its Traditionally Contradictory Enhancement by Nanotwin Boundary. *J. Phys. Chem. Lett.* **2018**, *9*, 5704–5709. [CrossRef]

18. Luo, Y.; Yang, X.; Feng, T.; Wang, J.; Ruan, X. Vibrational hierarchy leads to dual-phonon transport in low thermal conductivity crystals. *Nat. Commun.* **2020**, *11*, 2554. [CrossRef]

19. Ravindran, P.; Delin, A.; Ahuja, R.; Johansson, B.; Auluck, S.; Wills, J.M.; Eriksson, O. Optical properties of monoclinic SnI_2 from relativistic first-principles theory. *Phys. Rev. B* **1997**, *56*, 6851–6861. [CrossRef]

20. Zhong, M.; Zhang, S.; Huang, L.; You, J.; Wei, Z.; Liu, X.; Li, J. Large-scale 2D PbI_2 monolayers: Experimental realization and their indirect band-gap related properties. *Nanoscale* **2017**, *9*, 3736–3741. [CrossRef]

21. Yagmurcukardes, M.; Peeters, F.M.; Sahin, H. Electronic and vibrational properties of PbI_2: From bulk to monolayer. *Phys. Rev. B* **2018**, *98*, 085431. [CrossRef]

22. Zhang, Y.M.; Hou, B.; Wu, Y.; Chen, Y.; Xia, Y.-J.; Mei, H.; Kong, M.R.; Peng, L.; Shao, H.Z.; Cao, J.; et al. Towards high-temperature electron-hole condensate phase in monolayer tetrels metal halides: Ultra-long excitonic lifetimes, phase diagram and exciton dynamics. *Mater. Today Phys.* **2022**, *22*, 100604. [CrossRef]

23. Sandoval, S.; Kepic, D.; Perez Del Pino, A.; Gyorgy, E.; Gomez, A.; Pfannmoeller, M.; Tendeloo, G.V.; Ballesteros, B.; Tobias, G. Selective Laser-Assisted Synthesis of Tubular van der Waals Heterostructures of Single-Layered PbI_2 within Carbon Nanotubes Exhibiting Carrier Photogeneration. *ACS Nano* **2018**, *12*, 6648–6656. [CrossRef]

24. Peng, B.; Mei, H.D.; Zhang, H.; Shao, H.Z.; Xu, K.; Ni, G.; Jin, Q.Y.; Soukoulis, C.M.; Zhu, H.Y. High thermoelectric efficiency in monolayer PbI_2 from 300 K to 900 K. *Inorg. Chem. Front.* **2019**, *6*, 920–928. [CrossRef]

25. Fan, Q.; Huang, J.W.; Dong, N.N.; Hong, S.; Yan, C.; Liu, Y.C.; Qiu, J.S.; Wang, J.; Sun, Z.Y. Liquid Exfoliation of Two-Dimensional PbI_2 Nanosheets for Ultrafast Photonics. *ACS Photonics* **2019**, *6*, 1051–1057. [CrossRef]

26. Howie, R.A.; Moser, W.; Trevena, I.C. The crystal structure of tin(II) iodide. *Acta Crystallogr. B Struct. Sci. Cryst. Eng. Mater.* **1972**, *28*, 2965–2971. [CrossRef]

27. Yuan, Q.Q.; Zheng, F.; Shi, Z.Q.; Li, Q.Y.; Lv, Y.Y.; Chen, Y.; Zhang, P.; Li, S.C. Direct Growth of van der Waals Tin Diiodide Monolayers. *Adv. Sci.* **2021**, *8*, 2100009. [CrossRef]

28. Arab, A.; Li, Q. Anisotropic thermoelectric behavior in armchair and zigzag mono- and fewlayer MoS2 in thermoelectric generator applications. *Sci. Rep.* **2015**, *5*, 13706. [CrossRef]

29. Kresse, G.; Furthmuller, J. Efficient iterative schemes for ab initio total-energy calculations using a plane-wave basis set. *Phys. Rev. B Condens. Matter.* **1996**, *54*, 11169–11186. [CrossRef]

30. Blochl, P.E. Projector augmented-wave method. *Phys. Rev. B Condens. Matter* **1994**, *50*, 17953–17979. [CrossRef]

31. Blochl, P.E.; Jepsen, O.; Andersen, O.K. Improved tetrahedron method for Brillouin-zone integrations. *Phys. Rev. B Condens. Matter.* **1994**, *49*, 16223–16233. [CrossRef] [PubMed]

32. Kresse, G.; Joubert, D. From ultrasoft pseudopotentials to the projector augmented-wave method. *Phys. Rev. B* **1999**, *59*, 1758–1775. [CrossRef]

33. Heyd, J.; Scuseria, G.E. Assessment and validation of a screened Coulomb hybrid density functional. *J. Chem. Phys.* **2004**, *120*, 7274–7280. [CrossRef] [PubMed]

34. Madsen, G.K.H.; Singh, D.J. BoltzTraP. A code for calculating band-structure dependent quantities. *Comput. Phys. Commun.* **2006**, *175*, 67–71. [CrossRef]

35. Bardeen, J.; Shockley, W. Deformation Potentials and Mobilities in Non-Polar Crystals. *Phys. Rev.* **1950**, *80*, 72–80. [CrossRef]

36. Lee, M.S.; Mahanti, S.D. Validity of the rigid band approximation in the study of the thermopower of narrow band gap semiconductors. *Phys. Rev. B* **2012**, *85*, 165149. [CrossRef]

37. Cai, Y.; Zhang, G.; Zhang, Y.W. Polarity-reversed robust carrier mobility in monolayer MoS_2 nanoribbons. *J. Am. Chem. Soc.* **2014**, *136*, 6269–6275. [CrossRef]

38. Zhu, X.L.; Liu, P.F.; Zhang, J.; Zhang, P.; Zhou, W.X.; Xie, G.; Wang, B.T. Monolayer SnP_3: An excellent p-type thermoelectric material. *Nanoscale* **2019**, *11*, 19923–19932. [CrossRef]

39. Baroni, S.; de Gironcoli, S.; Dal Corso, A.; Giannozzi, P. Phonons and related crystal properties from density-functional perturbation theory. *Rev. Mod. Phys.* **2001**, *73*, 515–562. [CrossRef]

40. Togo, A.; Oba, F.; Tanaka, I. First-principles calculations of the ferroelastic transition between rutile-type and $CaCl_2$-typeSiO_2 at high pressures. *Phys. Rev. B* **2008**, *78*, 134106. [CrossRef]

41. Li, W.; Carrete, J.; Katcho, N.A.; Mingo, N. ShengBTE: A solver of the Boltzmann transport equation for phonons. *Comput. Phys. Commun.* **2014**, *185*, 1747–1758. [CrossRef]

42. Tong, Z.; Li, S.; Ruan, X.; Bao, H. Comprehensive first-principles analysis of phonon thermal conductivity and electron-phonon coupling in different metals. *Phys. Rev. B* **2019**, *100*, 144306. [CrossRef]

43. Li, S.; Wang, A.; Hu, Y.; Gu, X.; Tong, Z.; Bao, H. Anomalous thermal transport in metallic transition-metal nitrides originated from strong electron–phonon interactions. *Mater. Today Phys.* **2020**, *15*, 100256. [CrossRef]

44. Wang, Y.X.; Xu, N.; Li, D.Y.; Zhu, J. Thermal Properties of Two Dimensional Layered Materials. *Adv. Funct. Mater.* **2017**, *27*, 1604134. [CrossRef]

45. Peng, B.; Zhang, H.; Shao, H.; Xu, Y.; Zhang, R.; Lu, H.; Zhang, D.W.; Zhu, H. First-Principles Prediction of Ultralow Lattice Thermal Conductivity of Dumbbell Silicene: A Comparison with Low-Buckled Silicene. *ACS Appl. Mater. Interfaces* **2016**, *8*, 20977–20985. [CrossRef]

46. Onodera, T.; Morita, Y.; Nagumo, R.; Miura, R.; Suzuki, A.; Tsuboi, H.; Hatakeyama, N.; Endou, A.; Takaba, H.; Dassenoy, F.; et al. A computational chemistry study on friction of h-MoS(2). Part II. Friction anisotropy. *J. Phys. Chem. B* **2010**, *114*, 15832–15838. [CrossRef]

47. Zhao, L.D.; Zhang, X.; Wu, H.; Tan, G.; Pei, Y.; Xiao, Y.; Chang, C.; Wu, D.; Chi, H.; Zheng, L.; et al. Enhanced Thermoelectric Properties in the Counter-Doped SnTe System with Strained Endotaxial SrTe. *J. Am. Chem. Soc.* **2016**, *138*, 2366–2373. [CrossRef]

48. Wang, D.Y.; He, W.K.; Chang, C.; Wang, G.T.; Wang, J.F.; Zhao, L.D. Thermoelectric transport properties of rock-salt SnSe: First-principles investigation. *J. Mater. Chem. C* **2018**, *6*, 12016–12022. [CrossRef]

49. Huang, S.; Wang, Z.Y.; Xiong, R.; Yu, H.Y.; Shi, J. Significant enhancement in thermoelectric performance of Mg_3Sb_2 from bulk to two-dimensional mono layer. *Nano Energy* **2019**, *62*, 212–219. [CrossRef]

50. Wang, N.; Li, M.; Xiao, H.; Zu, X.; Qiao, L. Layered LaCuOSe: A Promising Anisotropic Thermoelectric Material. *Phys. Rev. Appl.* **2020**, *13*, 024038. [CrossRef]

51. Tong, Z.; Dumitrica, T.; Frauenheim, T. Ultralow Thermal Conductivity in Two-Dimensional MoO_3. *Nano Lett.* **2021**, *21*, 4351–4356. [CrossRef] [PubMed]

52. Zhu, X.-L.; Liu, P.-F.; Wu, Y.-Y.; Zhang, P.; Xie, G.; Wang, B.-T. Significant enhancement of the thermoelectric properties of CaP_3 through reducing the dimensionality. *Adv. Mater.* **2020**, *1*, 3322–3332. [CrossRef]

53. Liu, D.; Every, A.G.; Tománek, D. Continuum approach for long-wavelength acoustic phonons in quasi-two-dimensional structures. *Phys. Rev. B* **2016**, *94*, 165432. [CrossRef]

54. Lindsay, L.; Li, W.; Carrete, J.; Mingo, N.; Broido, D.A.; Reinecke, T.L. Phonon thermal transport in strained and unstrained graphene from first principles. *Phys. Rev. B* **2014**, *89*, 155426. [CrossRef]

55. Wang, H.; Zhou, E.; Duan, F.; Wei, D.; Zheng, X.; Tang, C.; Ouyang, T.; Yao, Y.; Qin, G.; Zhong, J. Unique Arrangement of Atoms Leads to Low Thermal Conductivity: A Comparative Study of Monolayer Mg_2C. *J. Phys. Chem. Lett.* **2021**, *12*, 10353–10358. [CrossRef]

56. Hippalgaonkar, K.; Wang, Y.; Ye, Y.; Qiu, D.Y.; Zhu, H.; Wang, Y.; Moore, J.; Louie, S.G.; Zhang, X. High thermoelectric power factor in two-dimensional crystals of MoS_2. *Phys. Rev. B* **2017**, *95*, 115407. [CrossRef]

57. Lin, H.; Tan, G.; Shen, J.N.; Hao, S.; Wu, L.M.; Calta, N.; Malliakas, C.; Wang, S.; Uher, C.; Wolverton, C.; et al. Concerted Rattling in CsAg5 Te3 Leading to Ultralow Thermal Conductivity and High Thermoelectric Performance. *Angew. Chem. Int. Ed. Engl.* **2016**, *55*, 11431–11436. [CrossRef]

58. Ma, N.; Li, Y.Y.; Chen, L.; Wu, L.M. alpha-CsCu5Se3: Discovery of a Low-Cost Bulk Selenide with High Thermoelectric Per formance. *J. Am. Chem. Soc.* **2020**, *142*, 5293–5303. [CrossRef]

59. Gibson, Q.D.; Zhao, T.; Daniels, L.M.; Walker, H.C.; Daou, R.; Hebert, S.; Zanella, M.; Dyer, M.S.; Claridge, J.B.; Slater, B.; et al. Low thermal conductivity in a modular inorganic material with bonding anisotropy and mismatch. *Science* **2021**, *373*, 1017–1022. [CrossRef]